ADVANCES IN ATMOSPHERIC SCIENCES, VOL. 33, AUGUST 2016, 996–1004

Distinctive Precursory Air–Sea Signals between Regular and Super El Niños

Lin CHEN[1,2], Tim LI*[1,2], Swadhin K. BEHERA[3], and Takeshi DOI[3]

[1] *Key Laboratory of Meteorological Disaster, Joint International Research Laboratory of Climate and Environmental Change,*
and Collaborative Innovation Center on Forecast and Evaluation of Meteorological Disasters,
Nanjing University of Information Science and Technology, Nanjing 210044

[2] *International Pacific Research Center, School of Ocean and Earth Science and Technology, University of Hawaii,*
2525 *Correa Rd., Honolulu, HI* 96822, *USA*

[3] *Application Laboratory, Japan Agency for Marine-Earth Science and Technology, Yokohama,* 236-0001, *Japan*

(Received 27 November 2015; revised 23 March 2016; accepted 11 April 2016)

ABSTRACT

Statistically different precursory air–sea signals between a super and a regular El Niño group are investigated, using observed SST and rainfall data, and oceanic and atmospheric reanalysis data. The El Niño events during 1958–2008 are first separated into two groups: a super El Niño group (S-group) and a regular El Niño group (R-group). Composite analysis shows that a significantly larger SST anomaly (SSTA) tendency appears in S-group than in R-group during the onset phase [April–May(0)], when the positive SSTA is very small. A mixed-layer heat budget analysis indicates that the tendency difference arises primarily from the difference in zonal advective feedback and the associated zonal current anomaly (u'). This is attributed to the difference in the thermocline depth anomaly (D') over the off-equatorial western Pacific prior to the onset phase, as revealed by three ocean assimilation products. Such a difference in D' is caused by the difference in the wind stress curl anomaly *in situ*, which is mainly regulated by the anomalous SST and precipitation over the Maritime Continent and equatorial Pacific.

Key words: super El Niño, precursory air–sea signals, thermocline depth anomaly, ENSO

Citation: Chen, L., T. Li, S. K. Behera, and T. Doi, 2016: Distinctive precursory air–sea signals between regular and super El Niños. *Adv. Atmos. Sci.*, **33**(8), 996–1004, doi: 10.1007/s00376-016-5250-8.

1. Introduction

ENSO is one of Earth's most important climate variabilities (Philander et al., 1984; Chao and Zhang, 1990), and its accurate prediction carries considerable socioeconomic impacts (Huang and Wu, 1989; Li, 1990; McPhaden, 1999). In early 2014, many climate models around the world predicted the occurrence of a super El Niño [here, this term stands for an extraordinarily strong El Niño (Hong et al., 2014; Latif et al., 2015), such as the 1997–98 El Niño] by the end of 2014 (e.g., Tollefson, 2014). However, the forecast of a 2014 super El Niño did not materialize.

The failure of the 2014 forecast poses an important issue for the ENSO research community; namely, what makes a super El Niño? Previous studies have proposed various hypotheses to explain what causes the different growth rate of such an El Niño event. For example, McPhaden (1999) suggested that atmospheric "noise" on synoptic–intraseasonal timescales may have played a role in the rapid onset of the 1997–98 El Niño. A series of modeling studies support the notion that westerly wind events (WWEs) help set up the favorable condition for a super El Niño to occur (Lengaigne et al., 2004; Vecchi and Harrison, 2006), with their role in the development of El Niño events having been further tested in recent studies (Hu et al., 2014; Menkes et al., 2014; Fedorov et al., 2015; Li et al., 2015; Chen et al., 2016). However, the occurrence of WWEs is not a solely sufficient condition for the occurrence of super El Niños, because WWEs also occur during regular and non-El Niño years. In fact, it has been argued that WWEs are not even a necessary condition for the occurrence of El Niño, because many ocean–atmosphere coupled models simulate ENSO variability without well-simulated WWEs (McPhaden, 1999). Moreover, WWEs tend to be more frequent and stronger during large warm events, implying that they are not purely stochastic—at least some WWEs depend strongly on the low-frequency state of ENSO (Eisenman et al., 2005; Gebbie et al., 2007; Rong et al., 2011; Chen et al., 2015a).

It is widely accepted that the buildup of heat content in the western Pacific is a precursor to El Niño events (Wyrtki, 1975; Wyrtki, 1985; Clarke, 2010; Kumar and Hu, 2014). However, it is not clear whether or not there is a statistically significant difference in the precursory signal between super

---

* Corresponding author: Tim LI
Email: timli@hawaii.edu

and regular El Niños. Ramesh and Murtugudde (2013) argued that similar precursor subsurface signals appear in the western equatorial Pacific prior to nearly all El Niño events. However, they only concentrated on the subsurface signals at the equator, ignoring the impact of off-equatorial signals on ENSO (Yu and Sun, 2009; Ding et al., 2015; Zheng et al., 2015).

Other factors that may affect El Niño intensity include the internal nonlinearity (Timmermann et al., 2003), oceanic nonlinear advection (Jin et al., 2003; Su et al., 2010), atmospheric nonlinearity associated with the SST threshold for deep convection (Takahashi and Dewitte, 2016) and noise-induced instability (Jin et al., 2007; Levine and Jin, 2010). It is not clear, however, how these nonlinear processes operate differently during regular and strong El Niños. Hong et al. (2014) suggested that anomalous low-level flow induced by a high pressure anomaly in the Southern Hemisphere (SH) is critical in accelerating El Niño growth in boreal summer. However, it is difficult to identify if such low-level wind anomalies are a cause or a result of a super El Niño, as by the boreal summer of super El Niño development, the warming in the eastern equatorial Pacific is already quite strong.

Most previous studies have focused on examining an individual El Niño case. As each El Niño event is very different (Chen et al., 2015a), it is necessary to examine their common features and the statistically significant differences between super and regular El Niño groups. In this respect, we focus in the present work on investigating the distinctive signals in both the atmosphere and ocean prior to the onset of El Niño events, as a small SST anomaly (SSTA) tendency difference during the onset phase can make a huge difference in the later developing stage, due to various positive atmosphere–ocean feedbacks (e.g., Philander et al., 1984; Hirst, 1988; Li, 1997).

The main objective of the current study is to reveal the fundamental differences in the precursory atmospheric and oceanic signals between super and regular El Niño groups. In section 2, the data and method are described. In section 3, we present the statistically significant signals for the two groups. A summary and discussion are given in section 4.

2. Data and method

The observational SST data used in this study are from ERSST.v3b (Smith et al., 2008). To obtain a sufficient amount of observed El Niño samples, the SODA (version 2.1.6) data (Carton and Giese, 2008) for the period 1958–2008 are used. SODA provides oceanic 3D temperature and velocity fields, the surface wind stress field, and sea surface height fields. The sea surface height datasets from the ECMWF's Ocean Reanalysis System 4 (ORA-S4; Balmaseda et al., 2013), covering the period 1958–2008, along with the NCEP GODAS data (Saha et al., 2006) for the period 1980–2008, are also used. To reduce the uncertainty of the surface heat flux data (Kumar and Hu, 2012), they are derived from the ensemble mean of the NCEP–NCAR Reanalysis-1 data (Kalnay et al., 1996) for the period 1958–2008, and the WHOI OAFlux data (Yu et al., 2008) for the period 1984–2008, in which the shortwave and longwave radiation flux are acquired from the ISCCP (Zhang et al., 2004). The composite analysis associated with precipitation data is derived from the ensemble mean of three datasets, including the precipitation reconstruction (PREC; Chen et al., 2002) dataset for the period 1958–2008, and the CMAP (Xie and Arkin, 1997) and GPCP (version 2.1; Huffman et al., 2009) data for the period 1979–2008.

Monthly anomalies are obtained by first subtracting the monthly mean climatology for the period 1958–2008; then, the Butterworth band-pass filter (Russell, 2006) is used to remove the high-frequency (< 6 months) and low-frequency (> 8 years) components.

The SSTA over the Niño3 region of (5°S–5°N, 150°–90°W) during November–January [ND(0)J(1)] exceeding 0.75 standard deviations (STDs) is considered as an El Niño event. Here, year(0) indicates the year of an El Niño event, and year(−1) and year(+1) indicate the preceding and following year, respectively. As shown in the time series of normalized Niño3 index (Fig. 1a), three El Niño events (72/73, 82/83, and 97/98) with amplitudes greater than 2.5 STDs can be classified into a super El Niño group, and the other eleven El Niño events (63/64, 65/66, 69/70, 76/77, 86/87, 87/88, 91/92, 94/95, 02/03, 04/05, and 06/07) into a regular El Niño group.

To investigate the specific dynamic and thermodynamic air–sea coupling processes in causing different SSTA tendencies during the onset phase, a mixed-layer heat budget analysis is conducted. The mixed-layer temperature tendency equation (Li et al., 2002; Wang et al., 2012) is

$$\begin{aligned}\frac{\partial T'}{\partial t} = & \underbrace{-u'\frac{\partial \overline{T}}{\partial x}}_{\text{term 1}} \underbrace{-\overline{u}\frac{\partial T'}{\partial x}}_{\text{term 2}} \underbrace{-u'\frac{\partial T'}{\partial x}}_{\text{term 3}} \underbrace{-w'\frac{\partial \overline{T}}{\partial z}}_{\text{term 4}} \underbrace{-\overline{w}\frac{\partial T'}{\partial z}}_{\text{term 5}} \underbrace{-w'\frac{\partial T'}{\partial z}}_{\text{term 6}} \\ & \underbrace{-v'\frac{\partial \overline{T}}{\partial y}}_{\text{term 7}} \underbrace{-\overline{v}\frac{\partial T'}{\partial y}}_{\text{term 8}} \underbrace{-v'\frac{\partial T'}{\partial y}}_{\text{term 9}} + \underbrace{\frac{Q'_{\rm net}}{\rho c_p H}}_{\text{term 10}} + R\ ,\end{aligned} \tag{1}$$

where u, v and w represent the three-dimensional oceanic current; T is the mixed-layer temperature; $(\ )'$ denotes the interannual anomaly variables; $\overline{(\ )}$ denotes the climatological mean variables; $Q_{\rm net}$ is the summation of net downward shortwave radiation absorbed in the mixed layer ($Q_{\rm sw}$), net downward surface longwave radiation, and surface latent and sensible heat fluxes (positive heat flux indicates heating moving into the ocean); R represents the residual term; ρ is the density of seawater; c_p is the specific heat of seawater; and H is the mixed-layer depth that varies in time and space. H is defined as the depth where ocean temperature is 0.8 °C lower than the surface, following Wang et al. (2012). All the budget terms in Eq. (1) are integrated from the surface to the mixed-layer depth. Considering the shortwave penetration below the mixed layer, the $Q_{\rm sw}$ absorbed in the mixed layer can be written as (Wang et al., 2012)

$$Q_{\rm sw} = Q_{\rm surf} - 0.47 Q_{\rm surf} e^{-0.04H}\ , \tag{2}$$

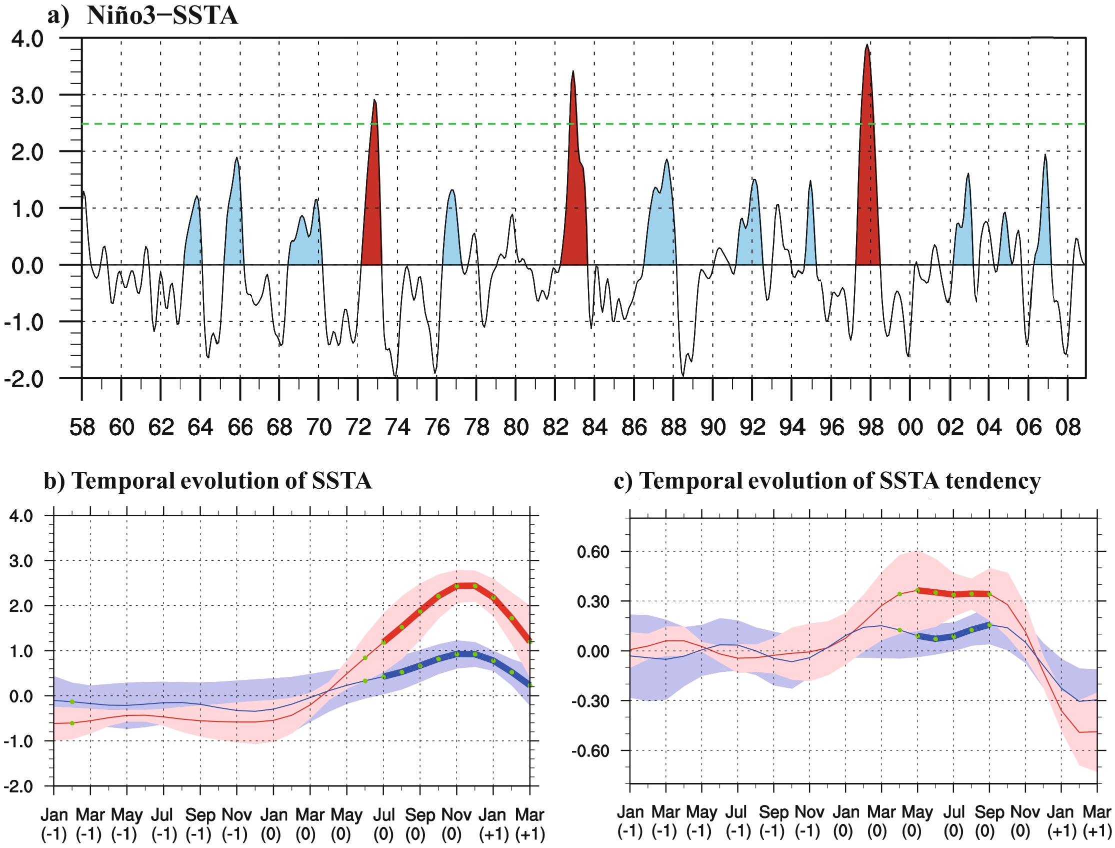

Fig. 1. (a) Time series of normalized Niño3 index obtained by using 6 months to 8 years band-pass-filtered SSTA derived from ERSST.v3b for the period 1958–2008. The green dashed line indicates the magnitude of 2.5 times STD. The red coloring indicates the super El Niño events (72/73, 82/83, and 97/98), and the blue indicates regular El Niño events. (b, c) Temporal evolutions of composite Niño3 SSTA (units: K) and SSTA tendency (units: K month^{-1}). The red (blue) line indicates the results derived from S-group (R-group), with shading representing the 1 STD spread of the samples within each group. Respectively, the green dots and thick lines indicate the difference between the two groups exceeding the 90% and 95% confidence level using the *t*-test. Here, year(0) indicates the El Niño event year, e.g., November–December(0)January(+1) corresponds to the peak phase of an El Niño event, with year(−1) or year(+1) indicating the preceding or following year, respectively.

where Q_{surf} is net downward surface shortwave radiation.

To understand the variation of the upper-ocean current anomaly, the anomalous geostrophic current and anomalous Ekman current are diagnosed. The zonal geostrophic current anomaly (u'_{g}) and zonal Ekman current anomaly (u'_{e}) are estimated as (Chen et al., 2015b)

$$u'_{\mathrm{g}} = -\frac{g\partial^2 D'}{\beta \partial y^2}\,, \tag{3}$$

$$u'_{\mathrm{e}} = \frac{1}{\rho H}\,\frac{r_{\mathrm{s}}\tau'_x + \beta y \tau'_y}{r_{\mathrm{s}}^2 + (\beta y)^2}\,, \tag{4}$$

where D', g and β are the thermocline depth anomaly, the reduced gravity, and the planetary vorticity gradient, respectively; τ'_x and τ'_y are the anomalous zonal and meridional wind stress; and r_{s} is the Rayleigh damping coefficient (0.5 d^{-1}) (Zebiak and Cane, 1987).

3. Results

3.1. *Distinctive SSTA tendencies during the onset phase of super and regular El Niño groups*

Figure 1a shows that, among the 14 El Niño events during 1958–2008, three super El Niño events (72/73, 82/83, 97/98) are apparent, and their amplitudes are much stronger than the average of the rest of the El Niño events. Figures 1b and c show the composite evolutions of the SSTA and SSTA tendency for the super El Niño group (S-group) and the regular El Niño group (R-group). It is noted that while the positive SSTAs are nearly zero in April(0) in both the S-group and R-group, there is a considerable difference in the SSTA tendencies between the two groups (Figs. 1b and c). Because of such a difference, the SSTAs in the two groups begin to bifurcate from April(0); that is, the positive SSTA increases rapidly in the following months and ultimately attains more than 2°C at the end of year(0) in S-group, whereas the positive

SSTA increases at a much slower rate and hardly exceeds 1 °C by end of year(0) in R-group.

Figure 1c shows that the average SSTA tendency in April–May(0) in S-group is more than two times greater than that in R-group. It is such a tendency difference during the onset phase that leads to the subsequent evolution difference. Thus, a key issue that needs to be addressed is the cause of the significantly large SSTA tendency difference during the onset phase [April–May(0)].

The tendencies of the mixed-layer temperature anomaly (MLTA) during the onset phase of the composite super and regular El Niño events are diagnosed, based on Eq. (1). Figures 2a and b show the mixed-layer heat budget terms for S-group and R-group. Here, the estimated MLTA tendency (i.e., term 11, which is the sum of terms 1–10), approximates the actual MLTA tendency (i.e., term 12), implying that the mixed-layer heat budget is approximately balanced. Note that the heat budget results by using different data and different approaches may produce different residual terms (Huang et al., 2010). Although the eddy process is not considered in this study, the dominant heat budget terms contributing to the El Niño development are similar to those revealed in previous studies (e.g., Huang et al., 2010). Figure 2c shows the difference in these budget terms between S-group and R-group (S minus R). Note that the most important term that contributes to the SSTA tendency difference between these two groups is term 1 ($-u'\partial\overline{T}/\partial x$), followed by term 5 ($-\overline{w}\partial T'/\partial z$). Respectively, these terms are the zonal advection of mean temperature by the zonal current anomaly, and the vertical advection of the anomalous temperature by the mean upwelling, denoting the well-known zonal advective feedback and thermocline feedback.

As both the zonal advective feedback and thermocline feedback involve the product of the mean and anomalous parts, we further examine their relative roles, using the total differentiation analysis approach proposed by Chen et al. (2015b). The result indicates that the main contributor is the anomaly part; that is, the zonal current anomaly (u') and the vertical gradient of anomalous temperature ($\partial T'/\partial z$). Thus, in the following analysis, we focus on examining the cause of the difference in u' and $\partial T'/\partial z$ during the onset phase between the two groups.

To investigate what causes the difference in u' between the two groups, we diagnose the zonal geostrophic current anomaly ($u'_{\rm g}$) and the zonal Ekman current anomaly ($u'_{\rm e}$) in an equatorial β-plane framework. Figure 2d displays the evolution of u', $u'_{\rm g}$ and $u'_{\rm e}$ at the equator derived from S-group (red curves) and R-group (blue curves). Indeed, u' during the

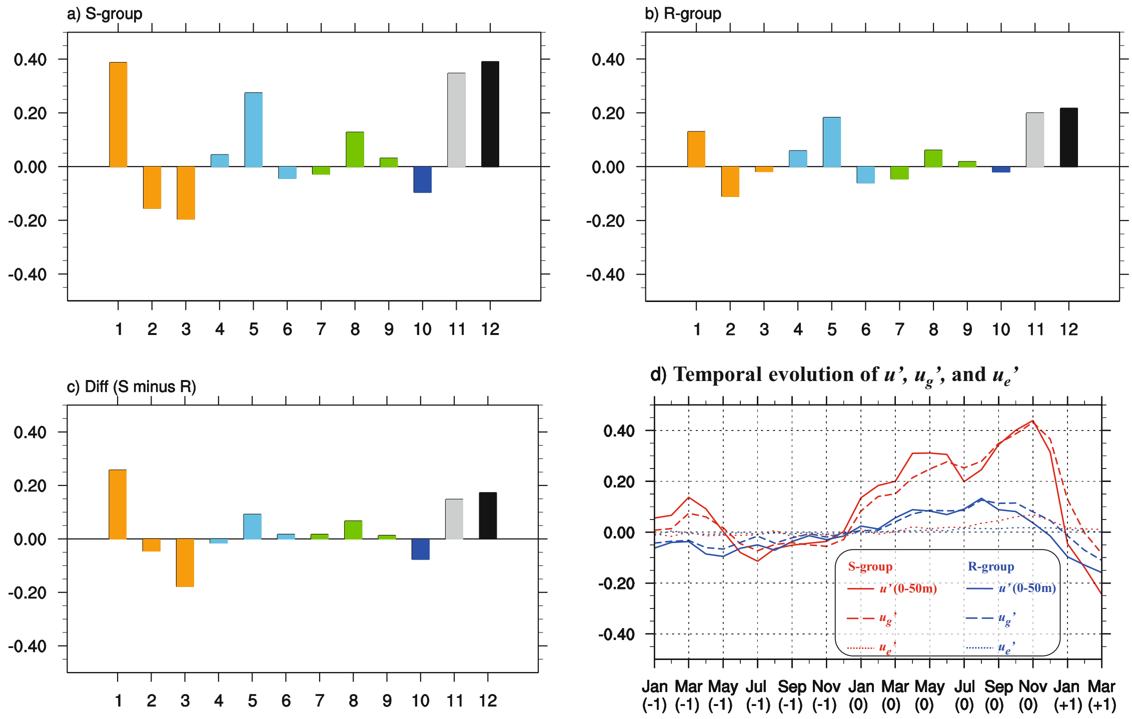

Fig. 2. The composite mixed-layer heat budget terms (units: K month^{-1}) during the onset phase [April–May(0)] from (a) S-group, (b) R-group and (c) the difference between S-group and R-group (using S minus R). Bar 12 denotes the mixed-layer temperature tendency $\partial T'/\partial t$, and bar 11 is the sum of all first 10 terms. The remaining terms are indicated by bar 1: $-u'\partial\overline{T}/\partial x$, bar 2: $-\overline{u}\partial T'/\partial x$, bar 3: $-u'\partial T'/\partial x$, bar 4: $-w'\partial\overline{T}/\partial z$, bar 5: $-\overline{w}\partial T'/\partial z$, bar 6: $-w'\partial T'/\partial z$, bar 7: $-v'\partial\overline{T}/\partial y$, bar 8: $-\overline{v}\partial T'/\partial y$, bar 9: $-v'\partial T'/\partial y$, and bar 10: $Q'_{\rm net}/\rho_0 C_{\rm p}H$. See the mixed-layer temperature tendency equation in section 2 for more details. (d) Temporal evolution of the composite zonal current anomaly (u'; m s^{-1}) averaged over 0–50 m, zonal geostrophic current anomaly (u'_g; m s^{-1}), and zonal Ekman current anomaly ($u'_{\rm e}$; m s^{-1}) along the equator (averaged over 2°S–2°N). The red and blue curves indicate S-group and R-group, respectively.

onset phase is stronger in S-group than in R-group. Note that the u' is mainly determined by u'_g, whereas the contribution of u'_e is much weaker. This is consistent with previous studies (e.g., Su et al., 2010, 2014; Chen et al., 2015b). Based on Eq. (3), u'_g is associated with the second meridional derivative of the thermocline depth anomaly (D'). Thus, a local maximum of D' at the equator would lead to an anomalous eastward geostrophic current. Additionally, previous studies have pointed out a close relationship between D' and $\partial T'/\partial z$; that is, a deepened thermocline (positive D') at the equator could induce the anomalous subsurface warming and thus a weakened stratification (e.g., Zebiak and Cane, 1987). This prompts us to further examine the difference in D' during the onset phase.

3.2. *Significant difference in the thermocline depth anomaly field*

To understand the cause of the D' difference during the onset phase, we investigate the evolution of D' from the pre-onset stage to the onset phase. Figure 3 shows the evolution of D' from June–July(−1) to April–May(0) in S-group and R-group, as well as their difference (S minus R). During JJ(−1)

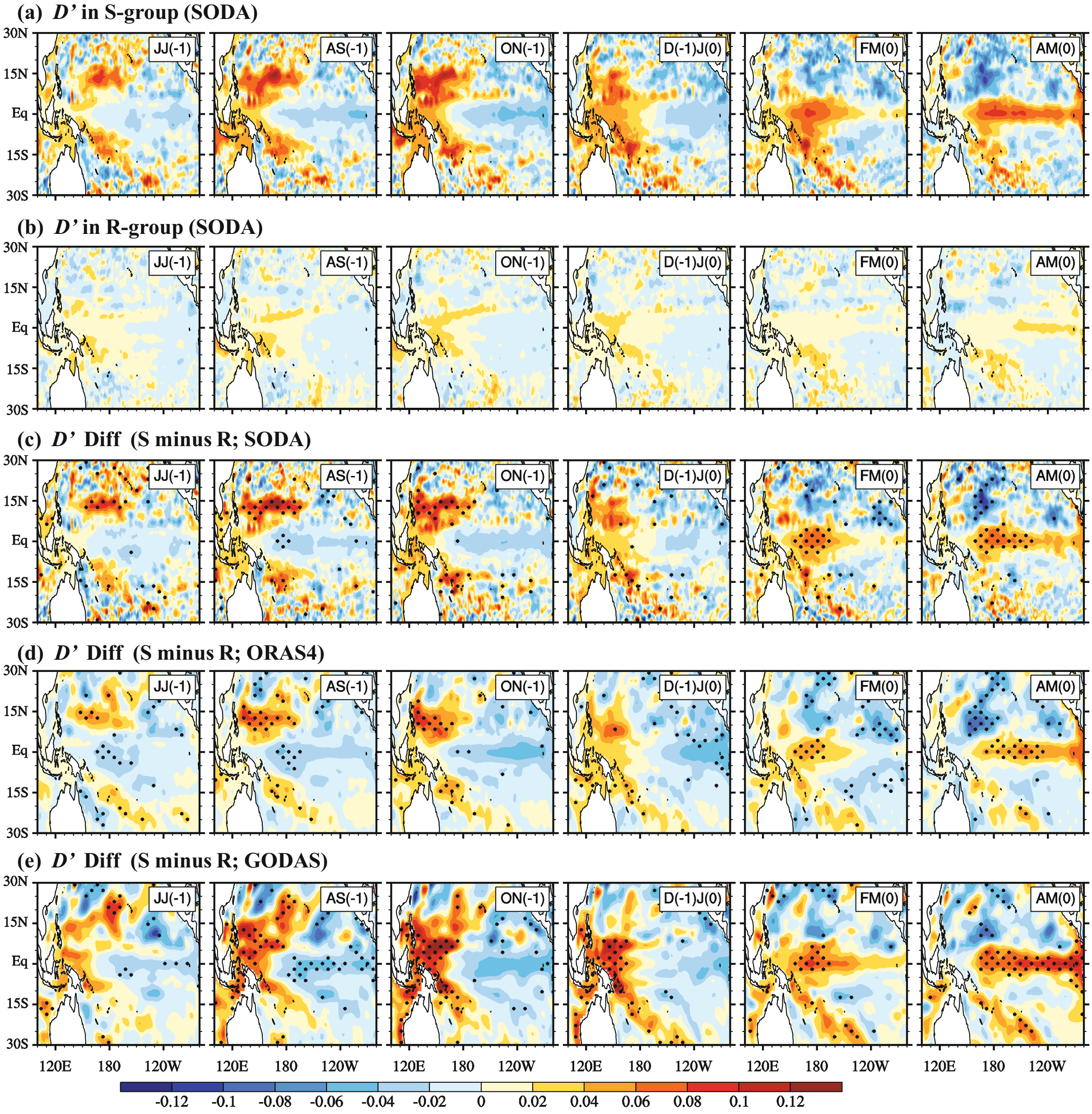

Fig. 3. The evolution of the composite SODA sea surface height anomaly (SSH′, units: m; a proxy of the thermocline depth anomaly, D') for June–July(−1), August–September(−1), October–November(−1), December(−1)January(0), February–March(0) and April–May(0), derived from (a) S-group, (b) R-group and (c) the difference between S-group and R-group. The stippling in each panel indicates the difference between S-group and R-group exceeding the 95% confidence level using the *t*-test. (d) As in (c) except for the ORA-S4 SSH′ data covering the period 1958–2008. (e) As in (c) except for the GODAS SSH′ data covering the period 1980–2008. Here, a linear D'–SSH′ relationship is applied.

to ON(−1), strong positive D' appears over the off-equatorial (10°–20°N and 10°–20°S) western Pacific region in S-group, while the D' over the off-equatorial western Pacific is significantly weak in R-group (Figs. 3a and b). In the subsequent months, the different D' signals over the off-equatorial region gradually propagate westward as Rossby waves and are reflected in the western boundary, resulting in a marked difference in the magnitude of D' at the equator in February–March(0) and April–May(0), i.e., much larger positive D' at the equator in S-group than R-group (Fig. 3c). Such a pronounced difference in the precursory D' signal is further confirmed by two other ocean products—ORA-S4 and GODAS (Figs. 3d and e). Thus, the accumulation of a deepened thermocline depth anomaly in the off-equatorial western Pacific in preceding months [June–September(−1)] holds the key for the differences in the thermocline depth, zonal current and vertical velocity anomalies in the subsequent months [i.e., February–March(0) and April–May(0)].

3.3. *What causes the difference in D' in the off-equatorial western Pacific?*

Further observational analysis shows that the significant difference in off-equatorial D' is primarily related to the difference in surface wind stress curl anomaly ($C'_{\rm url}$) between the two groups. During the pre-onset stage [June–July(−1) and August–September(−1)], anomalous negative $C'_{\rm url}$ appears over the off-equatorial western Pacific region of (8°–20°N, 130°E–160°W) in the Northern Hemisphere (NH), and anomalous positive $C'_{\rm url}$ appears over the off-equatorial western Pacific region of (8°–25°S, 150°E–160°W) in the SH. Here, "anomalous" stands for the difference between S-group and R-group (S minus R). Given the sign change of vorticity north and south of the equator, the opposite sign in $C'_{\rm url}$ between the NH and SH implies a pair of anomalous anticyclonic wind stress anomalies on both sides of the equator. As pointed out by Kessler (2006), $C'_{\rm url}$ is a major factor regulating D' in the off-equatorial western Pacific. Therefore, it is the distinctive wind stress anomaly that causes the marked difference in the thermocline depth anomaly between S-group and R-group in the off-equatorial western Pacific.

The twin anomalous anticyclonic wind stress fields shown in Fig. 4a during June–September(−1) are caused by the difference in the precipitation anomaly ($P'_{\rm r}$) and SST anomaly fields between S-group and R-group (Figs. 4b and c). Note that in June–September(−1), an anomalous positive $P'_{\rm r}$ appears over the Maritime Continent, and an anomalous negative $P'_{\rm r}$ appears in the western equatorial Pacific (near the dateline). The positive $P'_{\rm r}$ over the Maritime Continent, collocated with an underlying positive SSTA, can induce an atmospheric Kelvin wave response to its east (Wang and Li, 1993). As the amplitude of easterly anomalies associated with the Kelvin wave response decreases with latitude, an anticyclonic wind shear anomaly is generated in the off-equatorial western Pacific. Meanwhile, the negative precipitation anomaly near the dateline, caused by the cold SSTA in the central and eastern equatorial Pacific, can induce a pair of low-level anticyclonic Rossby gyres to the west of the negative heating region (Gill, 1980). Both the positive and negative precipitation/heating anomalies reinforce the twin anticyclonic wind stress anomaly in the off-equatorial western Pacific.

Examination of the SSTA evolution patterns shows that a La Niña–like pattern appears during June–September(−1) in both S-group and R-group (figure not shown). This indicates that the significant difference in Fig. 4c can be primarily attributed to the magnitude, not signal, of the SSTA. Both the positive SSTA over the Maritime Continent and the negative SSTA in the central and eastern equatorial Pacific are much stronger in S-group than in R-group. It is the distinctive east–west SSTA gradient that leads to the distinctive precipitation dipole shown in Fig. 4b.

Thus, the observational analysis reveals that the fundamental difference between the S- and R-group lies in the distinctive rainfall and SST anomaly patterns in the pre-onset stage [June–September(−1)]. A much stronger cooling (warming) in the eastern Pacific (Maritime Continent) leads to a distinctive dipole rainfall pattern, which further causes a significant difference in the off-equatorial $C'_{\rm url}$ and thermocline depth anomaly. The difference in the thermocline depth anomaly further leads to the distinctive SSTA tendencies in the eastern equatorial Pacific between the two groups during the onset phase.

4. Summary and discussion

This study investigates the statistically different precursory signals between groups of super and regular El Niños. For the period 1958–2008, fourteen El Niño events are identified and classified into two groups: a super El Niño group (including the 72/73, 82/83 and 97/98 El Niño events), and a regular El Niño group (including the rest of the El Niño events). Composite results show a significantly larger SSTA tendency in S-group than in R-group during the onset phase [April–May(0)] when the SSTA is nearly zero. A mixed-layer heat budget analysis shows that the difference in the SSTA tendencies during the onset phase is primarily caused by the difference in the zonal advective feedback and the associated zonal current anomaly.

Further diagnosis illustrates that the difference in the zonal current anomaly between S-group and R-group is primarily caused by the difference in the precursory signal of the thermocline depth anomaly (D') prior to the onset phase. As revealed by three sets of ocean reanalysis (i.e., SODA, ORA-S4 and GODAS), the difference in D' at the equator during the onset phase can be traced back to the precursory D' signals over the off-equatorial western Pacific during the preceding summer [June–September(−1)], when there is a significant difference in the curl of the wind stress anomaly field between the S- and R-group. From the perspective of difference fields (S minus R), a pair of anticyclonic anomalies appear in the off-equatorial western Pacific; and the wind stress anomalies are accompanied with positive precipitation and SST anomalies over the Maritime Continent and negative precipitation and SST anomalies over the central and eastern

(a) Wind stress C_{url}' Diff (S minus R)

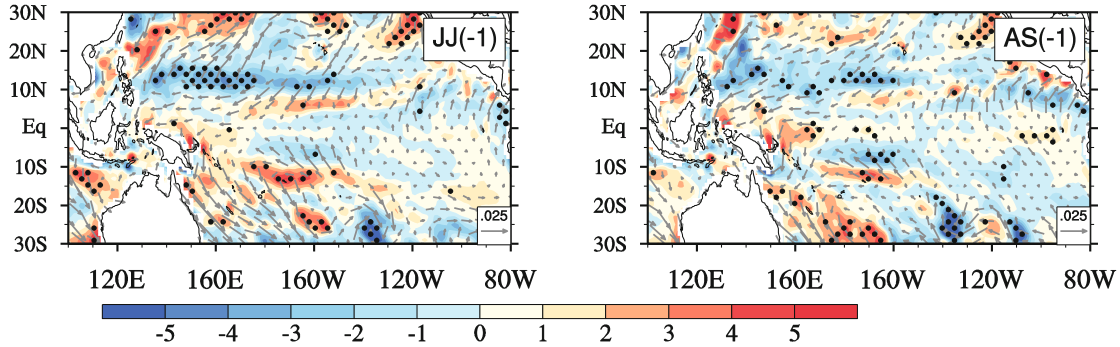

(b) P_r' Diff (S minus R)

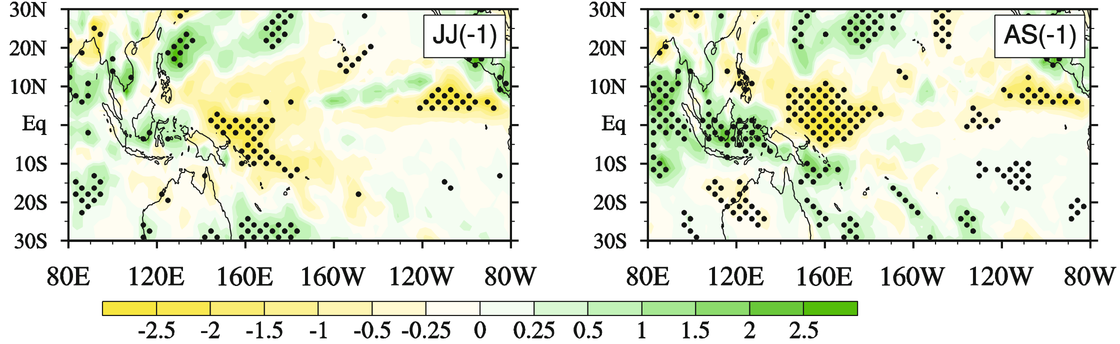

(c) *SSTA* Diff (S minus R)

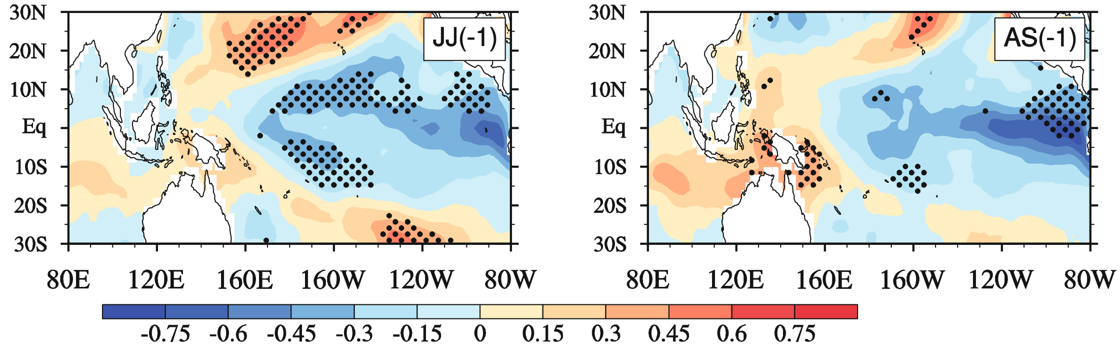

Fig. 4. The difference (using S minus R) in the composite (a) wind stress anomaly (vectors; units: N m^{-2}) and wind stress curl anomaly ($C'_{\rm url}$; shading; units: 10^{-8} N m^{-3}), (b) precipitation anomaly ($P'_{\rm r}$; mm d^{-1}), and (c) SSTA (units: K), for June–July(-1) and August–September(-1). The stippling in each panel indicates the difference between S-group and R-group exceeding the 95% confidence level using the *t*-test.

equatorial Pacific. Physically, it is argued that the anomalous anticyclonic gyres are the Rossby and Kevin wave responses to the anomalous dipole precipitation pattern.

Through the current observational analysis, we point out that the statistically different signals between super and regular El Niños appear in the pre-onset phase. Thus, special attention should be paid to the wind and thermocline anomalies over off-equatorial regions. On the other hand, significant SSTA tendencies between the S- and R-group also appear in the developing phase [say, June–September(0); Fig. 1c]. However, it becomes difficult to examine its cause, because of a lack of a clean way to filter out the impact from the pre-onset phase. Additionally, the D' field for each super and regular El Niño case is shown in Figs. S1 and S2 (see the electronic supplementary material). As one can see, for all three super El Niños, there is a clearly positive D' over the off-equatorial western Pacific during the pre-onset stage. Most of the regular El Niño cases have relatively weak or negative D' over the off-equatorial western Pacific, except a few regular El Niño events (e.g., 1965/66 and 1976/77), which followed strong La Niña events. With respect to the reason for the failed materialization of super El Niño in 1965/66 and 1976/77, it may be related to the lower temperature as the starting point due to the strong La Niña in advance, and the additional "prohibiting" processes, such as the occurrence of a series of easterly wind events (Hu and Fedorov, 2016) during the El Niño developing stage (figure not shown). Thus, a positive D' prior to the onset stage may not fully guarantee a super El Niño, because there might be a number of "prohibiting" processes operating during the El Niño developing phase. It is possible to identify certain "accelerating" or "prohibiting" processes during the El Niño developing phase for each individual case. For instance, the aforementioned WWEs (e.g., Fedorov et al., 2015) or the anomalous low-level equatorward flow (Hong et al., 2014) may accelerate the growth rate of SSTAs, and the negative SSTAs over the southeastern subtropical Pacific (Min et al., 2015) or easterly wind events (Hu and Fedorov, 2016) may prohibit El Niño development by suppressing the air–sea interaction. As "accelerating" or "prohibiting" processes could be different for different El Niño events, statistically significant signals may not necessarily be found. Nevertheless, such a case study is needed in order to fully understand the causal mechanisms underpinning a super El Niño.

Acknowledgements. We greatly acknowledge the three anonymous reviewers for their helpful comments and suggestions. We also acknowledge the data providers: ERSST.v3b, NCEP–NCAR, SODA, PREC, CMAP, GPCP and OAFlux data were obtained from http://apdrc.soest.hawaii.edu/dods/public_data. This study was jointly supported by the China National 973 Project (Grant No. 2015CB 453200), a Jiangsu Province project (Grant No. BK20150062), the NSFC (Grant Nos. 41475084, 41376002, and 41530426), the ONR (Grant No. N00014-16-12260), and the International Pacific Research Center sponsored by JAMSTEC. This paper is SOEST contribution number 9627, IPRC contribution number 1190, and ESMC contribution number 104.

Electronic supplementary material: Supplementary material is available in the online version of this article at http://dx.doi.org/10.1007/s00376-016-5250-8.

REFERENCES

Balmaseda, M. A., K. Mogensen, and A. T. Weaver, 2013: Evaluation of the ECMWF ocean reanalysis system ORAS4. *Quart. J. Roy. Meteor. Soc.*, **139**, 1132–1161.

Carton, J. A., and B. S. Giese, 2008: A Reanalysis of ocean climate using simple ocean data assimilation (SODA). *Mon. Wea. Rev.*, **136**, 2999–3017.

Chao, J. P., and R. H. Zhang, 1990: The air-sea interaction waves in the tropics and their instabilities. *Acta Meteorologica Sinica*, **48**, 46–54. (in Chinese)

Chen, D. K., and Coauthors, 2015a: Strong influence of westerly wind bursts on El Niño diversity. *Nature Geosci.*, **8**, 339–345.

Chen, L., T. Li, and Y. Q. Yu, 2015b: Causes of strengthening and weakening of ENSO amplitude under global warming in four CMIP5 models. *J. Climate*, **28**, 3250–3274.

Chen, L., Y. Q. Yu, and W.-P. Zheng, 2016: Improved ENSO simulation from climate system model FGOALS-g1.0 to FGOALS-g2, *Climate Dyn.*, 1–18, doi: 10.1007/s00382-016-2988-8.

Chen, M. Y., P. P. Xie, J. E. Janowiak, and P. A. Arkin, 2002: Global land precipitation: A 50-yr monthly analysis based on gauge observations. *J. Hydrometeor.*, **3**, 249–266.

Clarke, A. J., 2010: Analytical theory for the quasi-steady and low-frequency equatorial ocean response to wind forcing: The "tilt" and "warm water volume" modes. *J. Phys. Oceanogr.*, **40**, 121–137.

Ding, R. Q., J. P. Li, and Y.-H. Tseng, 2015: The impact of South Pacific extratropical forcing on ENSO and comparisons with the North Pacific. *Climate Dyn.*, **44**, 2017–2034.

Eisenman, I., L. Yu, and E. Tziperman, 2005: Westerly wind bursts: ENSO's tail rather than the dog? *J. Climate*, **18**, 5224–5238.

Fedorov, A. V., S. N. Hu, M. Lengaigne, and E. Guilyardi, 2015: The impact of westerly wind bursts and ocean initial state on the development, and diversity of El Niño events. *Climate Dyn.*, **44**, 1381–1401.

Gebbie, G., I. Eisenman, A. Wittenberg, and E. Tziperman, 2007: Modulation of westerly wind bursts by sea surface temperature: a semistochastic feedback for ENSO. *J. Atmos. Sci.*, **64**, 3281–3295.

Gill, A. E., 1980: Some simple solutions for heat-induced tropical circulation. *Quart. J. Roy. Meteor. Soc.*, **106**, 447–462.

Hirst, A. C., 1988: Slow instabilities in tropical ocean basin-global atmosphere models. *J. Atmos. Sci.*, **45**, 830–852.

Hong, L. C., LinHo, and F. F. Jin, 2014: A southern hemisphere booster of super El Niño. *Geophys. Res. Lett.*, **41**, 2142–2149.

Hu, S.-N., and A. V. Fedorov, 2016: Exceptionally strong easterly wind burst stalling El Niño of 2014. *Proc. Natl. Acad. Sci. U. S. A.*, **113**, 2005–2010.

Hu, S.-N., A. V. Fedorov, M. Lengaigne, and E. Guilyardi, 2014: The impact of westerly wind bursts on the diversity and predictability of El Niño events: an ocean energetics perspective. *Geophys. Res. Lett.*, **41**, 4654–4663, doi: 10.1002/2014 GL059573.

Huang, B.-Y., Y. Xue, D. X. Zhang, A. Kumar, and M. J. McPhaden, 2010: The NCEP GODAS ocean analysis of the tropical pacific mixed layer heat budget on seasonal to interannual time scales. *J. Climate*, **23**, 4901–4925.

Huang, R. H., and Y. F. Wu, 1989: The influence of ENSO on the summer climate change in China and its mechanism. *Adv. Atmos. Sci.*, **6**, 21–32, doi: 10.1007/BF02656915.

Huffman, G. J., R. F. Adler, D. T. Bolvin, and G. J. Gu, 2009: Improving the global precipitation record: GPCP version 2.1. *Geophys. Res. Lett.*, **36**, L17808.

Jin, F. F., S. I. An, A. Timmermann, and J. X. Zhao, 2003: Strong El Niño events and nonlinear dynamical heating. *Geophys. Res. Lett.*, **30**(3), 1120, doi: 10.1029/2002GL016356.

Jin, F. F., L. Lin, A. Timmermann, and J. Zhao, 2007: Ensemble-mean dynamics of the ENSO recharge oscillator under state-dependent stochastic forcing. *Geophys. Res. Lett.*, **34**, L03807, doi: 10.1029/2006GL027372.

Kalnay, E., and Coauthors, 1996: The NCEP/NCAR 40-year reanalysis project. *Bull. Am. Meteor. Soc.*, **77**, 437–471.

Kessler, W. S., 2006: The circulation of the eastern tropical Pacific: A review. *Progr. Oceanogr.*, **69**, 181–217.

Kumar, A., and Z. Z. Hu, 2012: Uncertainty in the ocean-atmosphere feedbacks associated with ENSO in the reanalysis products. *Climate Dyn.*, **39**, 575–588.

Kumar, A., and Z.-Z. Hu, 2014: Interannual and interdecadal variability of ocean temperature along the equatorial Pacific in conjunction with ENSO. *Climate Dyn.*, **42**, 1243–1258.

Latif, M., V. A. Semenov, and W. Park, 2015: Super El Niños in response to global warming in a climate model. *Climatic*

Change, **132**, 489–500.

Lengaigne, M., E. Guilyardi, J. P. Boulanger, C. Menkes, P. Delecluse, P. Inness, J. Cole, and J. Slingo, 2004: Triggering of El Niño by westerly wind events in a coupled general circulation model. *Climate Dyn*., **23**, 601–620.

Levine, A. F., and F.-F. Jin, 2010: Noise-induced instability in the ENSO recharge oscillator. *J. Atmos. Sci*., **67**, 529–542.

Li, C. Y., 1990: Interaction between anomalous winter monsoon in East Asia and El Niño events. *Adv. Atmos. Sci*., **7**, 36–46, doi: 10.1007/BF02919166

Li, J. Y., B. Q. Liu, J. D. Li, and J. Y. Mao, 2015: A comparative study on the dominant factors responsible for the weaker-than-expected El Niño event in 2014. *Adv. Atmos. Sci*., **32**, 1381–1390, doi: 10.1007/s00376-015-4269-6.

Li, T., 1997: Phase transition of the El Niño-southern oscillation: A stationary SST mode. *J. Atmos. Sci*., **54**, 2872–2887.

Li, T., Y. S. Zhang, E. Lu, and D. L. Wang, 2002: Relative role of dynamic and thermodynamic processes in the development of the Indian Ocean dipole: An OGCM diagnosis. *Geophys. Res. Lett*., **29**, 25-1–25-4.

McPhaden, M. J., 1999: Genesis and evolution of the 1997-98 El Niño. *Science*, **283**, 950–954.

Menkes, C. E., M. Lengaigne, J. Vialard, M. Puy, P. Marchesiello, S. Cravatte, and G. Cambon, 2014: About the role of westerly wind events in the possible development of an El Niño in 2014. *Geophys. Res. Lett.*, **41**, 6476–6483.

Min, Q. Y., J. Z. Su, R. H. Zhang, and X. Y. Rong, 2015: What hindered the El Niño pattern in 2014? *Geophys. Res. Lett*., **42**, 6762–6770, doi: 10.1002/2015GL064899.

Philander, S. G. H., T. Yamagata, and R. C. Pacanowski, 1984: Unstable air-sea interactions in the tropics. *J. Atmos. Sci*., **41**, 604–613.

Ramesh, N., and R. Murtugudde, 2013: All flavours of El Niño have similar early subsurface origins. *Nature Clim. Change*, **3**, 42–46.

Rong, X. Y., R. H. Zhang, T. Li, and J. Z. Su, 2011: Upscale feedback of high-frequency winds to ENSO. *Quart. J. Roy. Meteor. Soc*., **137**, 894–907.

Russell, D. R., 2006: Development of a time-domain, variable-period surface-wave magnitude measurement procedure for application at regional and teleseismic distances, Part I: Theory. *Bull. Seismol. Soc. Am*., **96**, 665–677.

Saha, S., and Coauthors, 2006: The NCEP climate forecast system. *J. Climate*, **19**, 3483–3517.

Smith, T. M., R. W. Reynolds, T. C. Peterson, and J. Lawrimore, 2008: Improvements to NOAA's historical merged land-ocean surface temperature analysis (1880–2006). *J. Climate*, **21**, 2283–2296.

Su, J. Z., R. H. Zhang, T. Li, X. Y. Rong, J. S. Kug, and C.-C. Hong, 2010: Causes of the El Niño and La Niña amplitude asymmetry in the equatorial eastern Pacific. *J. Climate*, **23**, 605–617.

Su, J. Z., B. Q. Xiang, B. Wang, and T. Li, 2014: Abrupt termination of the 2012 Pacific warming and its implication on ENSO prediction. *Geophys. Res. Lett*., **41**, 9058–9064.

Takahashi, K., and B. Dewitte, 2016: Strong and moderate nonlinear El Niño regimes. *Climate Dyn*., **46**, 1627–1645, doi: 10.1007/s00382-015-2665-3.

Timmermann, A., F.-F. Jin, and J. Abschagen, 2003: A nonlinear theory for El Niño bursting. *J. Atmos. Sci.*, **60**, 152–165.

Tollefson, J., 2014: El Niño tests forecasters. *Nature*, **508**, 20–21.

Vecchi, G. A., and D. E. Harrison, 2006: The termination of the 1997-98 El Niño. Part I: Mechanisms of oceanic change. *J. Climate*, **19**, 2633–2646.

Wang, B., and T. M. Li, 1993: A simple tropical atmosphere model of relevance to short-term climate variations. *J. Atmos. Sci*., **50**, 260–284.

Wang, L., T. Li, and T. J. Zhou, 2012: Intraseasonal SST variability and air-sea interaction over the Kuroshio extension region during boreal summer. *J. Climate*, **25**, 1619–1634.

Wyrtki, K., 1975: El Niño-the dynamic response of the equatorial Pacific Ocean to atmospheric forcing. *J. Phys. Oceanogr*., **5**, 572–584.

Wyrtki, K., 1985: Water displacements in the Pacific and the genesis of El Niño cycles. *J. Geophys. Res*.: *Oceans*, **90**, 7129–7132.

Xie, P. P., and P. A. Arkin, 1997: Global precipitation: A 17-year monthly analysis based on gauge observations, satellite estimates, and numerical model outputs. *Bull. Am. Meteor. Soc*., **78**, 2539–2558.

Yu, L., X. Jin, and R. A. Weller, 2008: Multidecade global flux datasets from the objectively analyzed air-sea fluxes (OAFlux) project: Latent and sensible heat fluxes, ocean evaporation, and related surface meteorological variables. OAFlux Project Technical Report OA-2008-01, 64 pp.

Yu, Y., and D.-Z. Sun, 2009: Response of ENSO and the mean state of the tropical Pacific to extratropical cooling and warming: A study using the IAP coupled model. *J. Climate*, **22**, 5902–5917.

Zebiak, S. E., and M. A. Cane, 1987: A model El Niño-southern oscillation. *Mon. Wea. Rev*., **115**, 2262–2278.

Zhang, Y. C., W. B. Rossow, A. A. Lacis, V. Oinas, and M. I. Mishchenko, 2004: Calculation of radiative fluxes from the surface to top of atmosphere based on ISCCP and other global data sets: Refinements of the radiative transfer model and the input data. *J. Geophys. Res*., **109**, D19105, doi: 10.1029/2003 JD004457.

Zheng, F., L. H. Feng, and J. Zhu, 2015: An incursion of off-equatorial subsurface cold water and its role in triggering the "double dip" La Niña event of 2011. *Adv. Atmos. Sci*., **32**, 731–742, doi: 10.1007/s00376-014-4080-9.